Versatile Motion Generation of Magnetic Origami Spring Robots in the Uniform Magnetic Field

Sishen Yuan , *Graduate Student Member, IEEE*, Sifan Cao, *Member, IEEE*,
Junnan Xue , *Graduate Student Member, IEEE*, Shijian Su , Junyan Yan ,
Min Wang, *Graduate Student Member, IEEE*, Wenchao Yue , Shing Shin Cheng , *Member, IEEE*, Jun Liu ,
Jiaole Wang , Shuang Song , Max Q.-H Meng , *Fellow, IEEE*, and Hongliang Ren , *Senior Member, IEEE*

Abstract—**Magnetic soft robots have attracted widespread attention for their untethered, remotely operated, and compliant deformation characteristics. Earlier work has demonstrated magnetic origami robots' diverse locomotion capabilities. This letter will focus on the motion generation and open-loop control of an untethered magnetic flexible robot with a stretch-twist coupling origami spring (OS) skeleton only using uniform magnetic field control. We investigate the associated motion generation mechanism and the corresponding control signals for the magnetic spring robot (MSR). The MSR can perform in-plane crawling (*Worm Crawling*) and perpendicular in-plane crawling (*Crab Crawling*) under two-dimensional magnetic signal inputs. Moreover, the OS's stretch-twist coupling characteristic is utilized to achieve axial *Rolling Motion* with axial magnetization configuration. We further experimentally tested the performance of three motions with average normalized velocities of 0.34±0.039(body length/s), 0.054±0.0066(body length/s), and 1.46±0.069(body length/s), respectively.**

Index Terms—**Magnetic spring robot (MSR), motion generation, worm crawling, crab crawling, rolling motion.**

Sishen Yuan, Sifan Cao, Shijian Su, Wenchao Yue, and Hongliang Ren are with the Department of Electronic Engineering, The Chinese University of Hong Kong, Hong Kong 999077, China (e-mail: yuansishen@outlook.com; caosifan002@163.com; shijiansu@fjirsm.ac.cn; wenchao.yue@link.cuhk.edu.hk; hlren@ieee.org).

Junnan Xue, Jiaole Wang, and Shuang Song are with the School of Mechanical Engineering and Automation, Harbin Institute of Technology (Shenzhen), Shenzhen 518055, China (e-mail: 20s153229@stu.hit.edu.cn; wangjiaole@hit.edu.cn; songshuang@hit.edu.cn).

Junyan Yan and Shing Shin Cheng are with the Department of Mechanical and Automation Engineering, The Chinese University of Hong Kong, Hong Kong 999077, China (e-mail: junyanyan@mae.cuhk.edu.hk; chengss90@gmail.com).

Min Wang and Jun Liu are with the Department of Mechanical Engineering, City University of Hong Kong, 999077, China (e-mail: wangmin_hit@outlook.com; jliu287@cityu.edu.hk).

Max Q.-H Meng is with the Department of Electronic and Electrical Engineering, Southern University of Science and Technology, Shenzhen 518055, China (e-mail: max.meng@ieee.org).

This letter has supplementary downloadable material available at https://doi.org/10.1109/LRA.2022.3194318, provided by the authors.

Digital Object Identifier 10.1109/LRA.2022.3194318

I. INTRODUCTION

CRAWLING locomotion mechanisms inspired by annelids and insect larvae have been applied to the motion generation of soft robots [1], performing tasks in complex spatial environments based on their deformation characteristics [2], [3]. Soft robotics actuation does not rely on discrete joints but rather utilizes the continuum modulation of softcomponents [4] such as elastomers, gels, fluids, and biomass. One of the challenges facing soft robots is the slow actuated velocity. Elastic instability has been revealed in rapidly reconfigurable structures [5] leading to buckling, wrinkling and snap-through behaviors [6]. Origami thus has become an alternative strategy for compliant reconfigurable robots to perform high-velocity motion [7].

Origami robot utilizes dynamically actuated folds on the body to assist with locomotion capabilities [8]. Christoph et al. proposed a modular origami robot called Mori, which is capable of moving on flat surfaces and attaching to other similar modules and can be folded into any desired 3D configuration [9]. Junius et al. presented an origami-inspired manipulator and compensated for the uncontrollable twisting typically present in continuum robots [10]. Felton. et al. developed a shape-memory composite material that folds itself along an embedded hinge, and an origami robot based on it can perform self-fold and walk away in less than 4 minutes without human intervention [11]. Other actuation methods for origami robots include magnetic actuation, optical actuation, expansion response actuation, pneumatic actuation [12] and so on.

The magnetic untethered soft robots are widely studied for in vivo applications for their ability to be operated remotely [13], [14]. Pham et al. presented a magnetic soft inchworm robot concept that can be exploited to produce controllable robotic therapeutic and diagnostic tools [15]. Steiner et al. extended the above work, and presented a detailed model and analysis of a magnetically actuated inchworm-like soft robot that can travel through a lumen environment [16]. Meanwhile, an organized, passive, compliant origami skeleton helps orient the robot's flexibility and deformation direction to simplify magnetic control. Our previous work constructed a library of actuatable structures by combining an origami letter skeleton with magnetized elastomers [17]. We also demonstrated the ability of magnetically actuated origami robots for generating various motions and performing functions [7], [18]. However, these works have only explored the response of magnetic origami robots to magnetic fields excited by permanent magnets, which is partly limited by the frequency of magnetic field changes and partly by the inability to avoid undesired perturbations caused
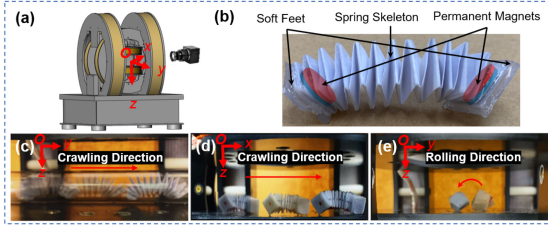
Fig. 1. Magnetic Origami Spring Robotic System. (a) 3D Helmholtz Actuation System. (b) MSR. (c) Worm Crawling Motion. (d) Crab Crawling Motion. (e) Rolling Motion.
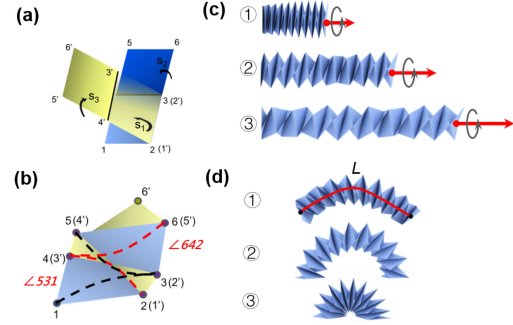

Fig. 2. Schematic diagram of the OS. (a) The folding process of the OS. (b) The vertical folded OS (VFOS) structure. (c) The stretch-twist coupling effect of OS under axial tension. Red arrows indicate the external gradually increasing tension, and gray arrows indicate the torque based on the stretch-twist coupling characteristic. (d) Effect of stretch-twist coupling on the bending of the OS.

by nonlinear magnetic forces. On the other hand, we cannot determine the specific contribution of magnetic torque and force in the generation of diverse motions. In other words, the advance of MSR sometimes cannot be ruled out if it relies on the influence of the attraction between the permanent magnets. Moreover, the magnetic torque actuation method tends to scale better with distance than magnetic force [19]. In this letter, a typical vertical folded generated OS (VFOS) structure, as shown in Fig. 1(b), is employed to construct the MSR and its motion generation in the uniform magnetic field, as shown in Fig. 1(a), with the symmetric axial magnetization configuration was studied. Bolei et al. connected a slinky to a pneumatic actuator and used an electromagnet and a plate embedded between the loops to initiate nonlinear pulsating movements [20]. The VFOS structure has tensile-torsional property and makes the minimum potential energy state of the MSR unique during bending. Based on this characteristic, we designed the input of a two-dimensional magnetic field signal to enable the MSR to generate three typical forms of motion: *Worm Crawling Motion* (Fig. 1(c)), *Crab Crawling Motion* (Fig. 1(d)), and *Rolling Motion* (Fig. 1(e)). The average velocity of the rolling motion is 51.13 mm/s, a competitive velocity compared to reported magnetic origami robots [7], [18], [21]. The main contributions of the work presented in this article are summarized as follows:

1) Design and fabrication of the untethered magnetic robot with OS as its skeleton;
2) Using only a two-dimensional uniform magnetic field (e.g., YOZ-plane signal input) to achieve *Worm Crawling Motion*, whose locomotion direction is along the Oy-axis. Its advantage is that only modulation $\mathbf{B}_y$ is required to achieve gait forward and backward, no special differentiation of the friction between the front and rear feet is required [21], and the steering does not require turning the entire body.
3) Only a two-dimensional uniform magnetic field (e.g., yOz-plane signal input) is utilized to achieve *Crab Crawling Motion*, whose locomotion direction is along the Ox-axis. It requires only around 50% of the magnetic field strength of *Worm Crawling Motion*. Thus *Crab Crawling Motion* would be an alternative actuating strategy in working areas with weak magnetic fields.
4) Realization of MSR's continuous rotation in the direction of magnetic moment with axial magnetization configuration via OS pull-torsion characteristics.

II. MAGNETIC OS ROBOTIC SYSTEM

A. Design of Magnetic Origami Robot

As shown in Fig. 1(b), the MSR consists of OS as the body with two co-axially embedded permanent magnets (diameter:

10 mm, height: 2 mm) mounted on both ends as the actuator with alternating magnetic polarity and axial magnetization [15], and silicone Ecoflex 00-10 as the skin of the feet. The natural extension length of MSR is 35 mm and 15 mm when fully compressed, and the final prototype weighs 2.1 g. For proof of concept, the OS was prepared on 80gsm A4 letter with Young's modulus of 190 MPa and a thickness t of 0.104 mm, and its geometric parameters included a square cross-sectional edge length a of 10 mm, and the number N of the recycled VFOS unit of 12.

Fig. 2(a) shows the steps of constructing the VFOS unit by folding and gluing the same size letter at a vertical angle. For each VFOS unit, as shown in Fig. 2(b), the elastic surface resists external forces and torques by its bending and stretching, and the bonding of two common edges of adjacent elastic surfaces makes it perform interlocking [22]–[24]. These features make the VFOS structure of a single repetitive unit with significant tensile-torsional coupling. Each VFOS unit has two mutually perpendicular switching angles, identified as $\angle 642$ and $\angle 531$, as shown in Fig. 2(b). Fig. 2(c) shows the morphological changes of the OS in a simulation environment as described in our earlier work [25] with one end fixed and under axial tension. Fig. 2(d) shows the morphological changes when the two ends of the OS are subjected to a coplanar reversal of equal torque.

B. Magnetic Actuation System

Experiments are performed using a 3D Helmholtz coil system shown in Fig. 1(a). The coils can generate 0.7mT/A, 0.73mT/A, and 1.33mT/A uniform magnetic fields within a space of 118 mm by 81 mm by 40 mm (x-axis, y-axis and z-axis), respectively. In such an approximately uniform magnetic field, the magnetic force is negligible, and the permanent magnet is subject only to the torque expressed as follows:

$$\mathbf{T} = \mathbf{m} \times \mathbf{B} \tag{1}$$

where $\mathbf{m}$ and $\mathbf{B}$ are the magnetic moment of the magnet and the magnetic flux density of the 3D Helmholtz coil system.

C. Internal Magnetic Interaction

Considering that two permanent magnets are installed at the ends of the MSR, it is necessary to determine the effect (positively or negatively) caused by their interaction, also called inter-agent force proposed in [26], in the generation of the motion. We denote the magnetic moments of the mounted magnets

by $\mathbf{m}_i$ and $\mathbf{m}_j$, and $\mathbf{n}_i$ and $\mathbf{n}_j$ denote the unit vectors of $\mathbf{m}_i$ and $\mathbf{m}_j$, respectively. We have, $\mathbf{m}_i = \frac{B_r}{\mu_0}\mathbf{n}_iV_i$, $\mathbf{m}_j = \frac{B_r}{\mu_0}\mathbf{n}_jV_j$, where $B_r = 1.3$T is the residual induction, $\mu_0 = 4\pi \times 10^{-7}$T $\cdot$ m·A^{-1} is the permeability of free space, V_i and V_j are the volumes of the magnets respectively. Explicitly, the force on the dipole $\mathbf{m}_j$ at location $\mathbf{p}_j$ from the dipole $\mathbf{m}_i$ at location $\mathbf{p}_i$ is [19]:

$$\mathbf{f}\{\mathbf{m}_j,\mathbf{p}_j,\mathbf{m}_i,\mathbf{p}_i\} = \frac{3\mu_0}{4\pi\|\mathbf{r}_{ij}\|^4}((\hat{\mathbf{r}}_{ij}^\top\mathbf{m}_j)\mathbf{m}_i + (\hat{\mathbf{r}}_{ij}^\top\mathbf{m}_i)\mathbf{m}_j$$
$$+ \left(\mathbf{m}_i^\top\mathbf{m}_j - 5(\hat{\mathbf{r}}_{ij}^\top\mathbf{m}_i)(\hat{\mathbf{r}}_{ij}^\top\mathbf{m}_j)\right)\hat{\mathbf{r}}_{ij}) \quad (2)$$

where $\mathbf{r}_{ij} = \mathbf{p}_j - \mathbf{p}_i$. The field of dipole $\mathbf{m}_i$ also impacts a torque on dipole $\mathbf{m}_j$:

$$\boldsymbol{\tau}\{\mathbf{m}_j,\mathbf{p}_j,\mathbf{m}_i,\mathbf{p}_i\} = \mathbb{S}\{\mathbf{m}_j\}\left(\frac{\mu_0(3\hat{\mathbf{r}}_{ij}\hat{\mathbf{r}}_{ij}^\top - \mathbb{I}_3)}{4\pi\|\mathbf{r}_{ij}\|^3}\right)\mathbf{m}_i \quad (3)$$

where $\mathbb{S}\{\mathbf{m}_j\}$ is the cross-product matrix mapping of the vector $\mathbf{m}_j$.

An incompressible rod is approximated instead of the OS to characterize the changes in magnetic interactions within the MSR during the bending process. We use the constant curvature model to describe the gradual bending of the MSR from a straight state to estimate the internal interaction forces (IMF) and torques (IMT). The permanent magnets at both ends are simplified as the magnetic dipole model. The internal magnetic reaction is simulated at two critical lengths ($L = 35$ mm, 45 mm), as shown in Fig. 2(d). The bending angle θ changes from 0 to π (0 represents the uncurved shape and π represents the semicircle shape). When θ is 0, i.e., the MSR is ideally straight, the IMF value is around $0.9 \times 10^{-3} \sim 2.2 \times 10^{-3}$N. As θ gradually increases, the value of IMF gradually increases until it reaches its maximum value at π, which is around 2.2×10^{-3}N $\sim 7 \times 10^{-3}$N. When θ is close to 0 or π, the IMT is close to the 0 N · m, so it does not cause any effect. But when θ is close to $\frac{2\pi}{3}$, the IMT gradually reaches its maximum value, which is around 0.42×10^{-5}N ·m $\sim 1.0 \times 10^{-5}$N · m. Here IMF and IMT values have been evaluated, and the magnitude of the magnetic field needs to be verified to be sufficient to avoid their effects, which will be addressed in the corresponding section.

III. MOTION GENERATION AND EXPERIMENTAL VALIDATION

A. Worm Crawling Motion

1) Locomotion Mechanism: For the MSR, the friction co-efficients at both ends are not deliberately treated, so a single signal of change in the z-axis direction does not effectively achieve MSR forward or backward. Often, the morphology is changed in situ. Inspired by the previous research [27]–[29], we expect to design a gait different from the conventional worm principle [15], [21], [28] to actuate the MSR utilizing an in-plane rotating magnetic field. Thus the input signal can be expressed as a superposition of two sine waves, which can be expressed theoretically as follows (taking y-axis and z-axis as an example)

$$\mathbf{B}_y = A_{B_y}sin\left(\omega t + \frac{\pi}{2}\right) + C_{B_y}$$
$$\mathbf{B}_z = A_{B_z}sin(\omega t) + C_{B_z} \quad (4)$$

TABLE I
ONE FEASIBLE SOLUTION FOR *WORM CRAWLING MOTION*

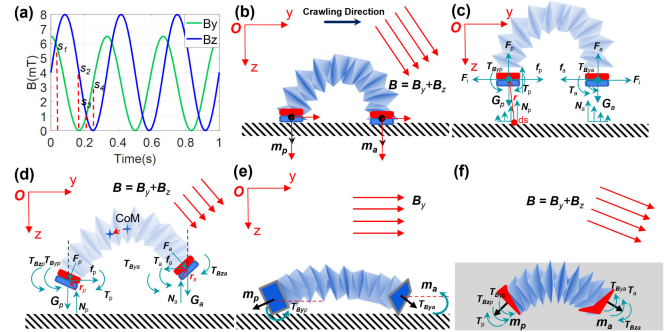| A_{B_y}(mT)	A_{B_z}(mT)	C_{B_y}(mT)	C_{B_z}(mT)	ω
3.25	4	3.25	4	6π

Fig. 3. Locomotion mechanism of the *Worm Crawling Motion*. (a) Two-dimensional magnetic field input signals. (b) A singular pose of the MSR in which the magnetic moments of the two magnets on the feet are perpendicular to the support surface. (c) The force and moment distribution at both feet as the MSR approaches state s_1. (d) The force and torque distribution of MSR during the transitional process from s_1 to s_3. (e) Since $\mathbf{B}_z = 0$, the torque of $\mathbf{B}_y$ will cause the MSR to be straightened. (f) MSR rapidly resumes its bent state storing elastic potential energy for the next motion cycle.

Since this rotating magnetic field only circulates in the quarter plane ($0° \sim 90°$), we set $A_{B_y} = C_{B_y}$, $A_{B_z} = C_{B_z}$. For the determination of magnetic field magnitude and frequency, we experimentally tested different combinations of magnetic field magnitude (0-10mT) and frequency (0-5 Hz) to obtain one feasible solution with a stable gait, as shown in Table I and Fig. 3(a). Although the same proportional increase in magnetic field magnitude and frequency also performs well, the choice here was based on the minimum energy consumption principle.

We define the anterior foot as the end in contact with the support surface located in front of the robot's motion direction and the other end as the posterior foot. We first consider the force analysis of the MSR under certain specific morphologies and magnetic fields. Fig. 3(b) shows a singular pose of the MSR in which the magnetic moments of the two magnets on the feet, denoted as $\mathbf{m}_p$ and $\mathbf{m}_a$, are perpendicular to the support surface. As the MSR approaches state s_1, the force and moment distribution at both feet can be simplified as shown in Fig. 3(c). Assuming that this process is quasi-static, the following equilibrium equation can be obtained:

$$\mathbf{G}_p = \mathbf{F}_p + \mathbf{N}_p; \mathbf{F}_i = \mathbf{f}_p = \mathbf{f}_a; \mathbf{G}_a = \mathbf{F}_a + \mathbf{N}_a$$

$$\mathbf{T}_p = \mathbf{T}_{B_yp} + \int_s \mathbf{n}_p \times \mathbf{r}ds; \int_s \mathbf{n}_a \times \mathbf{r}ds = \mathbf{T}_a + \mathbf{T}_{B_ya}$$

$$\mathbf{N}_p = \int_s \mathbf{n}_pds; \mathbf{N}_a = \int_s \mathbf{n}_ads \quad (5)$$

where $\mathbf{G}_p$ and $\mathbf{G}_a$ are the distribution of gravity at the ends of the magnet, which are unequal due to the offset of the center of mass (CoM); $\mathbf{F}_i$ is the internal interaction force between the magnets, can be estimated from (2); $\mathbf{F}_p$ and $\mathbf{F}_a$ are the contraction forces at the ends of the MSR after stretching; ideally, they are equal; $\mathbf{N}_p$ and $\mathbf{N}_a$ are the support forces at the two ends of the MSR, respectively, which are unevenly distributed due to the applied

torque, so that the support forces at unit contact area ds are defined as $\mathbf{n}_p$ and $\mathbf{n}_a$, respectively, and $\mathbf{r}$ is defined as the position vector from the ds position to the CoM of the magnet.

Obviously, when the MCR is in s_1, as shown in Fig. 3(b, c), the z-axis magnetic field produces almost no torque (not depicted in Fig. 3(b)) on the magnet since the angle between its direction and the magnetic moment is close to $0°$, and the static friction $\mathbf{f}_a$ and $\mathbf{f}_b$ maintain the current meso-stable shape. During the transitional process from s_1 to s_3, a transition state s_2 is chosen, as shown in Fig. 3(a), where $\| \mathbf{B}_z \| > \| \mathbf{B}_y \|$, and the force and torque distribution of MSR are shown in Fig. 3(d). As the torque generated by $\mathbf{B}_z$ is not enough for MSR to maintain bending, MSR needs to relax its body. Define the torque at the two ends of the MSR as $\mathbf{T}_p$ and $\mathbf{T}_a$, respectively, which can be expressed as follows (specify the counterclockwise direction as positive):

$$\mathbf{T}_p = \mathbf{T}_{\mathbf{B}_y p} + \mathbf{T}_{\mathbf{B}_z p} + \mathbf{N}_p \times \mathbf{r}_p - \mathbf{T}_p$$

$$\mathbf{T}_a = \mathbf{T}_{\mathbf{B}_y a} + \mathbf{T}_a - \mathbf{N}_a \times \mathbf{r}_a - \mathbf{T}_{\mathbf{B}_z a} \qquad (6)$$

where $\mathbf{r}_p$ and $\mathbf{r}_a$ are the position vectors of the contact point of the MSR with the support surface pointing to the CoM of magnets. Since $\mathbf{T}_p$ is greater than 0 and $\| \mathbf{T}_p \| > \| \mathbf{T}_a \|$, the CoM of the MSR will move backward (referring to the crawling direction) even if $\mathbf{T}_a$ is less than 0. If $\mathbf{T}_a$ is greater than 0, the backward shift of the center of mass will be more significant. Therefore, $\| \mathbf{N}_p \| > \| \mathbf{N}_a \|$. Moreover, the contact area S_p between $\mathbf{M}_p$ and the support surface is larger than that S_a between $\mathbf{M}_a$ and the support surface. Thus, $\| \mathbf{f}_p \| > \| \mathbf{f}_a \|$. As shown in Fig. 3(a), during s_2 to s_4, the $\| \mathbf{B}_z \|$ gradually decreases and MSR releases its elastic potential energy, explicitly identified as $\mathbf{F}_p$ and $\mathbf{F}_a$ in Fig. 3(d). Since there is less friction on the anterior foot, MSR relaxes its body and takes a step forward. In s_4, since $\mathbf{B}_z = 0$, the torque of $\mathbf{B}_y$ will cause the MSR to be straightened, as shown in Fig. 3(e). It is worth noting that the MSR has the smallest contact area with the support surface at this time. As $\mathbf{B}_z$ increases, MSR rapidly resumes its bent state storing elastic potential energy for the next motion cycle, as shown in Fig. 3(f).

The IMF may negatively affect the generation of s_1, considering that at this time, the IMF is a set of repulsive forces while its value gradually increases. The static friction coefficient between the MSR and the supporting surface is around 0.4. Since the prototype weighs 2.1 g, the static friction can reach 10.5×10^{-3}N, thus the negative impact of the IMF in the worst-case scenario is still not enough to resist the static friction, and this is also applicable to the *Rolling Motion*.

2) Experimental Gait Generation: Fig. 4 shows the motion sequence of MSR completing a single step in *Worm Crawling Motion*, which is divided into 6 frames. *Frame 1:* At the time t_1, the axial magnets of the anterior and posterior feet "grip" the support surface due to the simultaneous magnetic torque. The axis of the MSR is compressed in the gravitational direction and stretched upward to store elastic potential energy, as shown in Fig. 4(a). The static friction of the support surface contributes to maintaining morphological stability in the high-energy state. *Frame 2:* At the time t_2, the anterior foot is lifted first, resulting in a rapid decrease in the contact area of the support surface and the pressure, as shown in Fig. 4(b). *Frame 3:* However, the posterior foot still maintains sufficient contact with the support surface at this moment. Thus the elastic potential energy is released at the anterior foot, and the anterior foot is observed to move forward, as shown in Fig. 4(c). *Frame 4:* With the release of elastic energy, the robot relaxes its body, and the posterior foot turns into point
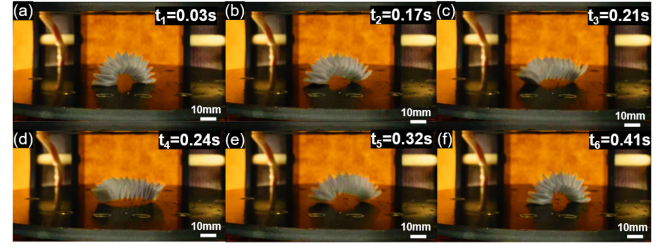

Fig. 4. Experimental Gait Generation - *Worm Crawling Motion* on the Plane. (a) The axial magnets of the anterior and posterior feet "grip" the support surface due to the simultaneous magnetic torque. (b) The anterior foot is lifted first, resulting in a rapid decrease in the contact area of the support surface and the pressure. (c) The elastic potential energy is released at the anterior foot, and the anterior foot is observed to move forward. (d) The robot relaxes its body, and the posterior foot turns into point contact with the support surface. (e) The anterior and posterior feet gradually approach each other to contract inward, storing the elastic potential energy again. (f) The friction between the anterior foot and the support surface is larger than that of the posterior foot due to the $\mathbf{B}_y$, so that the posterior foot can move forward.
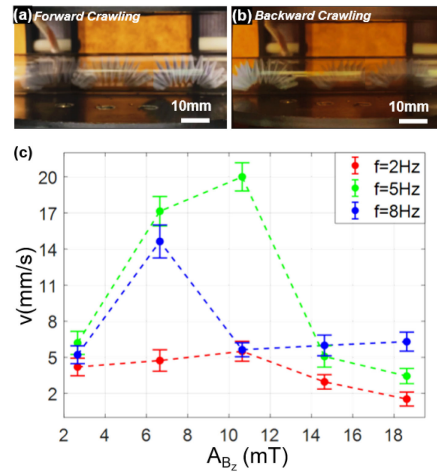

Fig. 5. *Worm Crawling Motion* in the Tube. (a) Forward Crawling. (b) Backward Crawling. (c) Effect of the A_{B_z}'s magnitude and frequency on motion velocity.

contact with the support surface, as shown in Fig. 4(d). *Frame 5:* At the time t_5, the anterior and posterior feet gradually approach each other to contract inward, storing the elastic potential energy again, as shown in Fig. 4(e). *Frame 6:* In this process, the friction between the anterior foot and the support surface is larger than that of the posterior foot due to the $\mathbf{B}_y$, so that the posterior foot can be observed to move forward, as shown in Fig. 4(f). (see **Supplementary Video**)

3) Motion in the Tube: Worm Crawling Motion is widely applied in the tube environment [15], [16], [21], [27]. To characterize its motion performance in the constraint environment, we placed an acrylic pipe with an inner diameter of 13*mm* in the workspace. We controlled the robot to perform motion in the designed direction. Moreover, we did not fix the ends of the acrylic pipe, which floated on the support surface. It would be a more demanding challenge since large and violent movements are not allowed in this case, considering that it would cause the pipe to roll unexpectedly. As shown in Fig. 5(a, b), the MSR enables forward and backward advancement in the tube. Because the control signal is unidirectional, only the value size varies, as
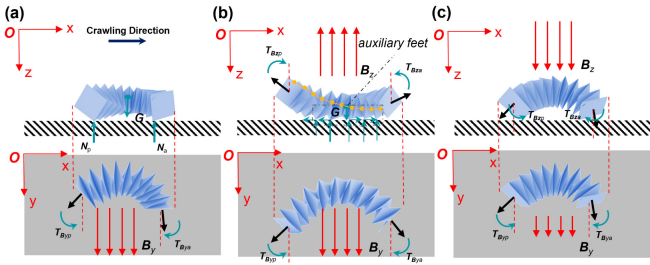
Fig. 6. Locomotion mechanism of the *Crab Crawling Motion*. (a) The MSR is initially axially parallel to the y-axis and designed with a unidirectional magnetic field $\mathbf{B}_y$ allowing the parallel state to be maintained. (b) The stretch-twist coupling characteristic of the OS shifts the CoM of the MSR to the right, giving the right half of the auxiliary feet more contact area with the support surface and more pressure, while the compliant adjustment of the VFOS unit switching angle brings all auxiliary feet closer to the middle of the MSR. (c) For a stretched MSR, the torque generated by $\mathbf{B}_z$ at its anterior and posterior feet makes its contact point with the support surface on the side of the anterior and posterior feet. During this process, the friction between the MSR and support surface is reduced due to the reduced contact area and changed friction coefficient. At the same time, the reduced $\mathbf{B}_y$ allows the MSR to release its stored elastic potential energy.

shown in Fig. 3(a), the MSR crawling direction can be switched by changing the direction of $\mathbf{B}_y$ (i.e., $B_y > 0$ for forward motion and $B_y < 0$ for backward motion).

We experimentally investigated the effect of the $\mathbf{B}_z$'s magnitude and frequency on the velocity of motion, as shown in Fig. 5(c). The best recorded performance of MSR worm crawling motion was 21.17 mm/s when $f = 5$ Hz, $A_{B_z} = 10.64$mT (i.e. $I = 8$ A). At a frequency of 5 Hz, the overall average velocity of MSR actuated by different A_{B_z} is higher than other frequencies. However, the optimal A_{B_z} varies for different frequencies, around 6.65∼10.64mT. The increase in magnetic field strength causes a decrease in velocity mainly because the diameter of the tube is very small, and the larger amplitude of the motion instead makes the back of the MSR and the upper wall of the tube produce resistance that prevents forward movement. The reason for the decrease in velocity caused by the increase in frequency mainly comes from the fact that the MSR's elastic potential energy release rate is lower than the change rate of the magnetic field, so the MSR does not move forward sufficiently in each stepping cycle before bending its body under the external magnetic field to store the elastic potential energy again.

B. Crab Crawling Motion

1) Locomotion Mechanism: For *Crab Crawling Motion*, we expect to design a crawling motion based on the conventional worm principle [15], [21], [28], but with the advantage of reducing the requirement for magnetic field magnitude as well as achieving motion in the perpendicular direction to the input signal plane while maintaining the same class of two-dimensional input signal as for *Worm Crawling Motion*. We define the contact points with the support surface other than the anterior foot and posterior foot at both ends of the MSR as the auxiliary foot, as shown in Fig. 6(b). To achieve Crab Crawling Motion, MSR needs to generate actuating friction in the direction of the body axis (Body axis refers to the CoM line of VFOS units that make up the MSR, and the spatial curve parallel to it is explicitly shown in Fig. 6(b), marked in yellow). The MSR should be initially axially parallel to the y-axis and designed with a unidirectional

magnetic field $\mathbf{B}_y$ allowing the parallel state to be maintained, as shown in Fig. 6(a). Since the anterior and posterior foot is heavier due to the mounted NdFeB magnets, they are support points in this state, while the auxiliary feet are not in contact with the support surface. Once the applied z-axis magnetic field generates torque to lift the anterior and posterior foot, it will force the auxiliary feet to become the support point, and as described previously, the VFOS unit switching angles undergoes a compliant adjustment to balance the external torque, as shown in Fig. 6(b). Furthermore, provided with the stretch-twist coupling characteristic of the OS, as depicted in Fig. 2(c), the left side of the MSR's body is lifted away from the supporting surface due to the internal torque since the spin direction in this configuration is along the Ox-axis (right-handed spiral rule). Similarly, the right half of the body of the MSR tends to be in contact with the supporting surface, although the magnet at the right end is subjected to an upward torque of $\mathbf{B}_z$, therefore shifting the CoM of the MSR to the right, giving the right half of the auxiliary feet more contact area with the support surface and more pressure, as shown in Fig. 6(b), while the compliant adjustment of the VFOS unit switching angle brings all auxiliary feet closer to the middle of the MSR. As a result, the auxiliary feet on the right half of the MSR's body generate greater sliding friction to move it forward a certain distance.

Another slight step forward may occur when we continuously increase the $\mathbf{B}_y$, allowing the MSR to store elastic potential energy, and $\mathbf{B}_z$ is controlled to change the way the MSR contacts the support surface (i.e., friction). It should be noted that the existence of this situation depends on whether the manufacturing process has deliberately differentiated the friction of the feet. As shown in Fig. 6(c), for a stretched MSR, the torque generated by $\mathbf{B}_z$ at its anterior and posterior feet makes its contact point with the support surface on the side of the anterior and posterior feet. During this process, the friction between the MSR and support surface is reduced due to the reduced contact area and changed friction coefficient, while the reduced $\mathbf{B}_y$ allows the MSR to release its stored elastic potential energy. Although the MSR would theoretically stretch on the sides of the axial body simultaneously, the difference in the composition of the silicone skin on the sides of the anterior and posterior feet causes different friction coefficients with the support surface in the fabricated MSR. As a result, the anterior foot will step forward a certain distance while the posterior foot will step forward at the beginning of the next movement cycle via the contraction of the OS skeleton. Based on the above analysis of the *Crab Crawling Motion* Mechanism, the input signal can be expressed theoretically as follows:

$$\mathbf{B}_y = A_{B_y} sin(\omega t) + C_{B_y}$$
$$\mathbf{B}_z = A_{B_z} sin(\omega t) + C_{B_z} \tag{7}$$

The phase difference between $\mathbf{B}_y$ and $\mathbf{B}_z$ is 0. And the magnitude of $\mathbf{B}_z$ needs to be limited. Otherwise, it will cause the MSR to form a shape similar to that of Worm Crawling Motion, which is undesired. As mentioned above, the determination of $\mathbf{B}_y$ needs to consider the impact of IMT and IMF. We experimentally tested different combinations of magnetic field magnitude (0-5mT) and frequency (0-5 Hz) to obtain a set of input signal parameters with a stable gait as shown in Table II and Fig. 7(a).

Among these three motions, the *Crab Crawling Motion* is designed to be in a weaker external magnetic field. The maximum actuated magnetic field value is only 4mT, which is 50% of the

TABLE II
ONE FEASIBLE SOLUTION FOR *CRAB CRAWLING MOTION*

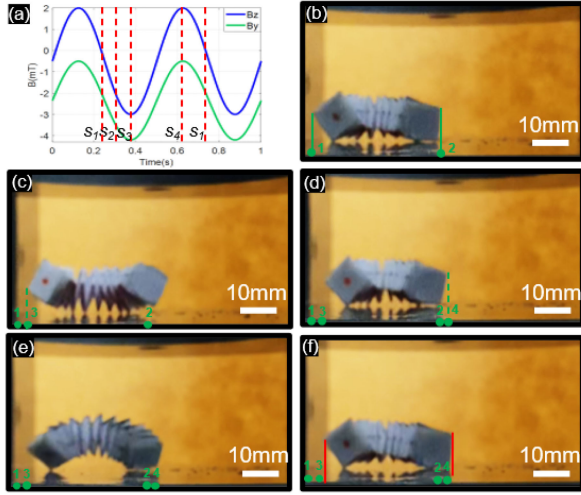| A_{B_y} (mT)	A_{B_z} (mT)	C_{B_y} (mT)	C_{B_z} (mT)	ω
1.85	2.5	-2.35	-0.5	4π

Fig. 7. (a) The input two-dimensional magnetic field signal of the *Crab Crawling Motion*. (b)-(f) Experimental Gait Generation - *Crab Crawling Motion*. Green markers 1 and 2 indicate the initial anterior and posterior feet projection positions; green markers 3 and 4 indicate the anterior and posterior feet projection positions after the first step forward; red vertical markers indicate the anterior and posterior feet projection positions after completing one cycle of step forward.

Worm Crawling Motion, so we only discuss the effect of IMT on the *Crab Crawling Motion* here. In this case, the bending of the MSR is mainly dependent on the torque provided by the magnetic field $\mathbf{B}_y$, thus we calculate that when the magnetic field $B_y = 4.2$mT, the angle between the magnetic field and the magnet is experimentally known to be about $15°$, which leads to a magnetic torque of 1.76×10^{-4}N·m, approximately 10 times that of IMT. In other words, this is also the basis for determining the value of the actuation magnetic field to be sufficient to avoid the influence of IMT and it has been experimentally proven to be feasible.

2) Experimental Gait Generation: Fig. 7 shows the motion sequence of MSR completing a single step in *Crab Crawling Motion*, which is divided into 4 frames. *Frame 1:* The robot is subjected to the y-axis magnetic field $\mathbf{B}_y$ only, labeled s_1 in Fig. 7(a), anterior and posterior feet are serving as support points while making the axial magnets at both ends as aligned as possible with the y-axis direction, as shown in Fig. 7(b). *Frame 2:* The robot rotates axially due to the increase in the magnitude of the magnetic field $\mathbf{B}_z$ (negative direction), labeled s_2 in Fig. 7(a), which generates an isotropic torque at both ends of the robot. In this process, anterior and posterior feet gradually leave the support surface. In contrast, the auxiliary feet start to support the robot, where the auxiliary feet are not symmetrical and cause uneven distribution of friction, as shown in Fig. 7(c). *Frame 3:* $B_y = -4.2$mT reaches the peak and $B_z = -3$mT, labeled s_3 in Fig. 7(a), the torque generated by By has the dominant effect and the robot returns to the front and rear foot support state, as shown in Fig. 7(d). *Frame 4:* As $\mathbf{B}_z$ increases (the sign "-" indicates the opposite of the defined positive direction), anterior and posterior feet generation tipping moments that reduce the contact area with
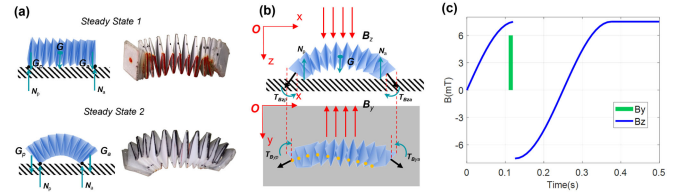

Fig. 8. Locomotion mechanism of the *Rolling Motion*. (a) The common states in the magnetic field-free environment for the MSR with the main mass distribution at both ends. (b) The torque generated by the transient $\mathbf{B}_y$ causes the CoM to deviate from the line of support points. It generates an overturning moment that takes the MSR out of its steady-state 2. (c) The input two-dimensional magnetic field signal of the *Rolling Motion* locomotion mechanism.

the support surface (leading to a decrease in static friction) and $\mathbf{B}_y$ gradually decreases to a minimum, labeled s_4 in Fig. 7(a), the robot's elastic potential energy is released, and the body is elongated. Due to manufacturing differences, the friction force of the anterior foot is less than that of the posterior foot, thus making the posterior foot remain motionless. In contrast, the anterior foot moves forward in the process, as shown in Fig. 7(e). As shown in Fig. 7(f), the $\mathbf{B}_z$ gradually decreases and the robot returns to its original shape for the next stepping cycle. (see **Supplementary Video**)

C. Rolling Motion

1) Locomotion Mechanism: The MSR crawling motion is adept at advancing through narrow and tortuous environments, but its movement velocity is limited. In the flat environment, rolling is more efficient than sliding (covering *Worm Crawling Motion* and *Crab Crawling Motion*.) For designs with axial magnets at both ends, there is generally a lack of a way for the robot to roll in the direction of the magnetic moment, for the external magnetic field is unable to generate torque in this direction [30]. However, the strong stretch-twist coupling of the OS would enable the axial magnetization configuration to achieve axial rotation. Before analyzing the mechanism of the *Rolling Motion*, we need to understand the steady-state of the MSR in terms of force (torque) generation and potential energy. The MSR with the main mass distribution at both ends is shown in Fig. 8(a). For steady-state 1, the COM of the anterior and posterior feet is closer to the MSR's CoM than the support point so that there is no bending moment at the ends of the MSR to stretch it, and it remains in a stable natural extension. It should be noted that although the MSR is close to a rectangle with a square cross-section, it is not isotropic because of the choice made when fabricating the anterior and posterior feet. Similarly, the selective fabricating processing results in a difference in the number of switching angles along the MSR body line, which leaves only one of the four body lines in the MSR's stretched state in a stable state, as will be explained later. For steady-state 2, the gravity of the anterior and posterior feet creates a bending moment stretching the MSR to form an arch due to insufficient supporting torques. As mentioned before, MSR is not isotropic, and the lowest potential energy in the stretched state is unique. Firstly, the bending of the MSR is coupled with stretching and twisting, but it is worth noting that ideally, if the MSR is bent along the body line, no twisting occurs, with the upper body line stretching and the lower body line gathering, as shown in Fig. 2(d). Furthermore, as mentioned before, the number of

TABLE III
ONE FEASIBLE SOLUTION FOR *ROLLING MOTION*

A_{B_z} (mT)	A_{B_y} (mT)	ω	t_1(s)	t_2(s)
7.5	6	4π	0.125	0.375

MSR's switching angles is n for one of the body lines and n-1 for the remaining three-body lines for the selective fabrication. Therefore, the extra "opening and closing angle" gives the MSR a lower gravitational potential energy and results in the lowest overall potential energy. In addition to steady-state 1 and steady-state 2 described above, there are still several mesostable states in the MSR. A sufficient magnetic field $\mathbf{B}_z$ generates a magnetic moment that will force these mesostable states, as well as stable state 1 to stable state 2, because of the bending process of the MSR, which causes stretching and a torsional torque that causes the MSR to tumble, in the direction of the spin of the OS. Likewise, controlling the direction of the magnetic field $\mathbf{B}_z$ will control the rolling direction.

In fact, with only the magnetic field $\mathbf{B}_z$, the MSR rolls over at most once in one direction or repeatedly in both directions with an unbiased sinusoidal input field $\mathbf{B}_z$. To avoid the MSR always falling into a steady-state 2 at the current position and not achieving a continuous unidirectional roll, discrete transient magnetic field $\mathbf{B}_y$ is introduced, as shown in Fig. 8(b). Since $\mathbf{B}_z$ makes the MSR an arch and raises its CoM, the torque generated by the transient $\mathbf{B}_y$ causes the CoM to deviate from the line of support points and generates an overturning moment that takes the MSR out of its steady-state 2. Based on the above analysis of the *Rolling Motion* mechanism, the input signal can be expressed theoretically as follows:

$$\mathbf{B}_z = A_{B_z} sin(\omega t), t \in [0, t_1]$$
$$\mathbf{B}_z = A_{B_z} sin(\omega t + \pi), t \in [t_1, t_2]$$
$$\mathbf{B}_y = A_{B_y}, t \in [t_1, t_1 + 0.01] \qquad (8)$$

Compared to the other two motions, *Rolling Motion* performs more stably because it relies mainly on the single signal B_z. Here we would like to provide a set of input signal parameters with a stable gait as shown in Table III and Fig. 8(c). However, these parameters are not unique or optimal. We just generalize a feasible combination based on the previous experimental data. And increasing these coefficients in the same proportion causes higher motion velocities. Still, given the limited working space, the experimentally measured velocities may not be sufficient to characterize the average velocity.

2) Experimental Gait Generation: Fig. 9 shows the transient state of MSR in the control sequence of Fig. 8(c), which is divided into 4 periods covering 12 frames. *Period 1:* The MSR is in steady-state 2 due to the torque applied by $\mathbf{B}_z$ ($B_z > 0$), and the transient $\mathbf{B}_y$ ($B_y > 0$) shifts the MSR's anterior and posterior feet slightly to the right, causing its CoM shifting to the left, and the MSR begins to roll to the left due to the gravitational torque. *Period 2:* Meanwhile, the switched direction of $\mathbf{B}_z$ will force the current non-stationary MSR to rapidly shift to the steady-state 2, which intuitively exhibits a continued roll to the left. *Period 3:* The $\mathbf{B}_z$'s switch direction again, causing the MSR to change its scrolling direction to the right. *Period 4:* The high-velocity characteristic of the *Rolling Motion* makes its inertia large and tends to cross the steady-state 2 briefly, but
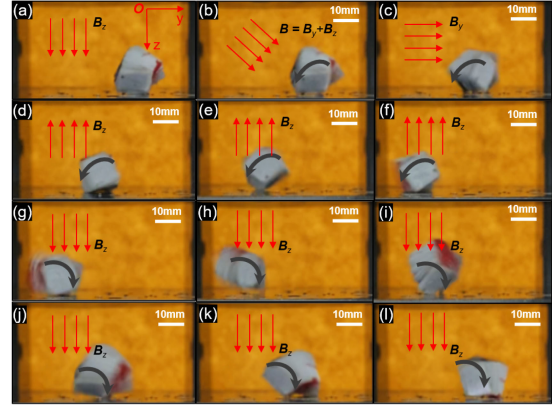

Fig. 9.   Experimental Gait Generation - *Rolling Motion*. (a)-(c) The transient $\mathbf{B}_y$ ($B_y > 0$) shifts the MSR's anterior and posterior feet slightly to the right, and the MSR begins to roll to the left due to the gravitational torque. (d)-(f) The $\mathbf{B}_z$ ($B_z < 0$) forces the current non-stationary MSR to rapidly shift to the steady-state 2. (g)-(i) The $\mathbf{B}_z$ ($B_z > 0$) causes the MSR to change its scrolling direction to the right. (j)-(l) The high velocity characteristic of the *Rolling Motion* makes its inertia large and tends to cross the steady-state 2 briefly, but eventually remains stationary due to the continuous $\mathbf{B}_z$ ($B_z > 0$).

TABLE IV
AVERAGE VELOCITY AND NORMALIZED VELOCITY

Motion	Average horizontal velocity (mm/s)	Normalized horizontal velocity (body length/s)
Worm Crawling on the plane	12.01	0.34
Worm Crawling (in the tube)	11.25	0.32
Crab Crawling	1.89	0.054
Rolling	51.13	1.46

TABLE V
COMPARISON OF MAGNETIC SOFT CRAWLING ROBOTS

Ref.	Year	Average horizontal velocity(mm/s)	Normalized horizontal velocity(body length/s)
[21]	2022	13.2	0.48
[27]	2021	38.8	0.4
[7]	2020	11.52	0.15
[15]	2020	8.7	0.29
[28]	2020	2.1	0.0875
[29]	2019	1.67	0.0418
[31]	2018	0.64	0.0376

eventually remains stationary due to the continuous $\mathbf{B}_z$. (see **Supplementary Video**)

D. Discussion

Table IV tabulates the normalized velocity as defined by

$$v_n = \frac{\bar{v}}{l_n} \qquad (9)$$

where v_n is the normalized velocity, $\bar{v}$ is the average velocity and l_n refers to the MSR's natural length. Table V gives the results of magnetic soft crawling robots in recent years. Both average velocity and normalized velocity of MSR are comparable or superior to most of the velocities achieved by the other works.

IV. Conclusion

This letter designed and analyzed a magnetic untethered robot adopting the OS as its backbone with comprehensive experimental evaluation. The motion response of the MSR in the uniform magnetic field was analyzed, and a two-dimensional magnetic field input signal was designed to actuate the robot to generate various motions. MSR achieved the *Worm Crawling Motion* which is coplanar with the input signal and the *Crab Crawling Motion* which is perpendicular to the input signal. Moreover, the OS's stretch-twist coupling characteristic is utilized to achieve axial *Rolling Motion* of the robot with axial magnetization configuration. The locomotion mechanism of the above motion has been analyzed to enable better modulation of the input signal. The velocity performance of MSR in different forms of motion was also measured experimentally, and the *Rolling Motion* had a significant advantage with an average normalized velocity of 1.46 ± 0.069(body length/s). *Worm Crawling Motion* also had a competitive normalized velocity, 0.34 ± 0.039(body length/s) compared to previous work. Although *Crab Crawling Motion* moved slowly with a velocity of 0.054 ± 0.0066(body length/s), it has the potential to achieve independent control of magnetically controlled crowds.

References

[1] J.-S. Koh and K.-J. Cho, "Omegabot: Crawling robot inspired by ascotis selenaria," in *Proc. IEEE Int. Conf. Robot. Automat.*, 2010, pp. 109–114.

[2] L. Qin et al., "A versatile soft crawling robot with rapid locomotion," *Soft Robot.*, vol. 6, no. 4, pp. 455–467, 2019.

[3] C. Xu, Z. Yang, S. W. K. Tan, J. Li, and G. Z. Lum, "Magnetic miniature actuators with six-degrees-of-freedom multimodal soft-bodied locomotion," *Adv. Intell. Syst.*, vol. 4, no. 4, 2021, Art. no. 2100259.

[4] M. Manti, V. Cacucciolo, and M. Cianchetti, "Stiffening in soft robotics: A review of the state of the art," *IEEE Robot. Automat. Mag.*, vol. 23, no. 3, pp. 93–106, Sep. 2016.

[5] S. Coyle, C. Majidi, P. LeDuc, and K. J. Hsia, "Bio-inspired soft robotics: Material selection, actuation, and design," *Extreme Mechanics Lett.*, vol. 22, pp. 51–59, 2018.

[6] B. S. Yeow et al., "Origami-inspired snap-through bistability in parallel and curved mechanisms through the inflection of degree four vertexes," in *Proc. IEEE Int. Conf. Robot. Automat.*, 2021, pp. 10863–10869.

[7] C. J. Cai et al., "Diversified and untethered motion generation via crease patterning from magnetically actuated caterpillar-inspired origami robot," *IEEE/ASME Trans. Mechatron.*, vol. 26, no. 3, pp. 1678–1688, Jun. 2021.

[8] D. Rus and C. Sung, "Spotlight on origami robots," *Sci. Robot.*, vol. 3, no. 15, 2018, Art. no. eaat0938.

[9] C. H. Belke and J. Paik, "Mori: A modular origami robot," *IEEE/ASME Trans. Mechatron.*, vol. 22, no. 5, pp. 2153–2164, Oct. 2017.

[10] J. Santoso and C. D. Onal, "An origami continuum robot capable of precise motion through torsionally stiff body and smooth inverse kinematics," *Soft Robot.*, vol. 8, no. 4, pp. 371–386, 2021.

[11] S. Felton, M. Tolley, E. Demaine, D. Rus, and R. Wood, "A method for building self-folding machines," *Science*, vol. 345, no. 6197, pp. 644–646, 2014.

[12] T. Jin et al., "Origami-inspired soft actuators for stimulus perception and crawling robot applications," *IEEE Trans. Robot.*, vol. 38, no. 2, pp. 748–764, Apr. 2022.

[13] J. A. Steiner, O. A. Hussain, L. N. Pham, J. J. Abbott, and K. K. Leang, "Toward magneto-electroactive endoluminal soft (MEESo) robots," in *Proc. Dyn. Syst. Control Conf.*, 2019, vol. 59162, Art. no. V003T20A002.

[14] Y. Kim, H. Yuk, R. Zhao, S. A. Chester, and X. Zhao, "Printing ferromagnetic domains for untethered fast-transforming soft materials," *Nature*, vol. 558, no. 7709, pp. 274–279, 2018.

[15] L. N. Pham, J. A. Steiner, K. K. Leang, and J. J. Abbott, "Soft endoluminal robots propelled by rotating magnetic dipole fields," *IEEE Trans. Med. Robot. Bionics*, vol. 2, no. 4, pp. 598–607, Nov. 2020.

[16] J. A. Steiner, L. N. Pham, J. J. Abbott, and K. K. Leang, "Modeling and analysis of a soft endoluminal inchworm robot propelled by a rotating magnetic dipole field," *J. Mechanisms Robot.*, vol. 14, no. 5, 2022, Art. no. 051002.

[17] B. S. Yeow et al., "Magnetically steerable serial and parallel structures by mold-free origami templating and domain setting," *Adv. Mater. Technol.*, vol. 7, no. 6, 2022, Art. no. 2101140.

[18] M. Sivaperuman Kalairaj et al., "Untethered origami worm robot with diverse multi-leg attachments and responsive motions under magnetic actuation," *Robotics*, vol. 10, no. 4, 2021, Art. no. 118.

[19] J. J. Abbott, E. Diller, and A. J. Petruska, "Magnetic methods in robotics," *Annu. Rev. Control, Robot., Auton. Syst.*, vol. 3, pp. 57–90, 2020.

[20] B. Deng, L. Chen, D. Wei, V. Tournat, and K. Bertoldi, "Pulse-driven robot: Motion via solitary waves," *Sci. Adv.*, vol. 6, no. 18, 2020, Art. no. eaaz1166.

[21] Q. Ze et al., "Soft robotic origami crawler," *Sci. Adv.*, vol. 8, no. 13, 2022, Art. no. eabm7834.

[22] T. Yoneda, D. Matsumoto, and H. Wada, "Structure, design, and mechanics of a letter spring," *Phys. Rev. E*, vol. 100, no. 1, 2019, Art. no. 013003.

[23] B.-H. Sun, "Universal scaling law of an origami letter spring," *Theor. Appl. Mechanics Lett.*, vol. 9, no. 6, pp. 409–412, 2019.

[24] Q. Chen, F. Feng, P. Lv, and H. Duan, "Origami spring-inspired shape morphing for flexible robotics," *Soft Robot.*, 2021.

[25] R. Swaminathan, C. J. Cai, S. Yuan, and H. Ren, "Multiphysics simulation of magnetically actuated robotic origami worms," *IEEE Robot. Automat. Lett.*, vol. 6, no. 3, pp. 4923–4930, Jul. 2021.

[26] M. Salehizadeh and E. Diller, "Three-dimensional independent control of multiple magnetic microrobots via inter-agent forces," *Int. J. Robot. Res.*, vol. 39, no. 12, pp. 1377–1396, 2020.

[27] H. Niu et al., "Magworm: A biomimetic magnet embedded worm-like soft robot," *Soft Robot.*, vol. 8, no. 5, pp. 507–518, 2021.

[28] D. Hua, X. Liu, S. Sun, M. A. Sotelo, Z. Li, and W. Li, "A magnetorheological fluid-filled soft crawling robot with magnetic actuation," *IEEE/ASME Trans. Mechatron.*, vol. 25, no. 6, pp. 2700–2710, Dec. 2020.

[29] E. B. Joyee and Y. Pan, "A fully three-dimensional printed inchworm-inspired soft robot with magnetic actuation," *Soft Robot.*, vol. 6, no. 3, pp. 333–345, 2019.

[30] E. Diller, J. Giltinan, G. Z. Lum, Z. Ye, and M. Sitti, "Six-degree-of-freedom magnetic actuation for wireless microrobotics," *Int. J. Robot. Res.*, vol. 35, no. 1–3, pp. 114–128, 2016.

[31] H. Lu et al., "A bioinspired multilegged soft millirobot that functions in both dry and wet conditions," *Nature Commun.*, vol. 9, no. 1, pp. 1–7, 2018.